

# SDSS AGNs with X-ray Emission from ROSAT PSPC Pointed Observations

A. A. Suchkov<sup>1</sup>, R. J. Hanisch<sup>2</sup>, W. Voges<sup>3</sup>, and T. M. Heckman<sup>1</sup>

## ABSTRACT

We present a sample of 1744 of Type 1 AGNs from the Sloan Digital Sky Survey Data Release 4 (SDSS DR4) spectroscopic catalog with X-ray counterparts in the White-Giommi-Angelini catalog (WGACAT) of ROSAT PSPC pointed observations. Of 1744 X-ray sources, 1410 (80.9%) are new AGN identifications. Of 4574 SDSS DR4 AGNs for which we found radio matches in the catalog of radio sources from the Faint Images of the Radio Sky at Twenty cm Survey (FIRST), 224 turned up in our sample of SDSS X-ray AGNs. The sample objects are given in a catalog that contains optical and X-ray parameters and supporting data, including redshifts; it also contains radio emission parameters where available. We illustrate the content of our catalog and its potential for AGN science by providing statistical relationships for the catalog data. The potential of the morphological information is emphasized by confronting the statistics of optically resolved, mostly low-redshift AGNs with unresolved AGNs that occupy a much wider redshift range. The immediate properties of the catalog objects include significant correlation of X-ray and optical fluxes, which is consistent with expectations. Also expected is the decrease of X-ray flux toward higher redshifts. The X-ray-to-optical flux ratio for the unresolved AGNs exhibits a decline toward higher redshifts, in agreement with previous results. The resolved AGNs, however, display the opposite trend. The X-ray hardness ratio shows a downward trend with increasing low-energy X-ray flux and no obvious dependence on redshift. At a given optical brightness, X-ray fluxes of radio-loud AGNs are on average higher than those of radio-quiet AGNs by a factor of 2. We caution, however, that because of the variety of selection effects present in both the WGACAT and the SDSS, the interpretation of any relationships based on our sample of X-ray AGNs requires a careful analysis of these effects.

*Subject headings:* catalogs—galaxies: active—galaxies: starbursts—quasars: general—radio continuum: galaxies—X-ray: galaxies

---

<sup>1</sup>Department of Physics and Astronomy, Johns Hopkins University, 3400, North Charles Street, Baltimore, MD 21218.

<sup>2</sup>Space Telescope Science Institute, operated by AURA Inc., under contract with NASA, 3700 San Martin Dr., Baltimore, MD 21218

<sup>3</sup>Max-Planck-Institut für extraterrestrische Physik, 85748 Garching, Germany

## 1. Introduction

Active galactic nuclei (AGNs)<sup>1</sup> produce X-ray emission as the gaseous material of a galaxy is accreted onto the massive black hole in its center. This emission provides powerful diagnostics to probe the inner working of the AGN central engines, and X-ray studies of AGNs at different redshifts have always been of fundamental importance for understanding the physics, origin, and evolution of these objects. X-ray data become especially informative when combined with optical data and redshift information, and there is much effort to build and analyze such samples. Thus, Fiore et al. (2003), presented optical identifications from the HELLAS2XMM survey for 122 sources detected with XMM-Newton in the surveyed area of 0.9 square degree. Green et al. (2004) found 335 unique optical counterparts for X-ray sources in the fields included in Chandra Multiwavelength Project (ChAMP), which is a survey of serendipitous Chandra X-ray sources in a  $\sim 14$  square degree field (Kim et al. 2004a). Half of the 125 counterparts that Green et al. (2004) classified spectroscopically proved to be broad-line AGNs and 40% turned out to be galaxies with narrow emission lines or absorption-line galaxies.

Along with designated optical follow-ups, much work was done to identify X-ray counterparts for AGNs detected in various optical and infrared surveys. Some of these surveys, such as that presented by Wolf et al. (2004) for the Chandra Deep Field South, specifically targeted the fields observed in X rays. Others serendipitously overlap with the fields from various X-ray missions. Particularly important for AGN studies is the Sloan Digital Sky Survey, which not only increased the number of known AGNs by an order of magnitude but also furnished redshifts and spectra. Many thousands of AGNs were spatially resolved, so a large amount of morphological information on underlying galaxies became available, too. A catalog of  $\sim 1200$  SDSS AGNs from the Early Data Release with X-ray counterparts from the ROSAT All Sky Survey (RASS; Voges et al., 1999; 2000) was presented by Anderson et al. (2003); this number nearly tripled for SDSS DR3 AGNs (Shen et al. 2005). The online system ClassX, developed by McGlynn et al. (2004; see also <http://heasarc.gsfc.nasa.gov/classx>), uses Virtual Observatory protocols<sup>2</sup> to retrieve optical information from other major surveys, such as 2MASS and USNO B1, and provides object type classifications using artificial intelligence algorithms. Most of the previously unidentified ROSAT X-ray sources are classified by ClassX as AGNs. Yet most of the X-ray sources detected by ROSAT, Chandra, XMM-Newton, and other large X-ray missions lack optical identifications.

There is a wide range of issues that can be addressed with samples of AGNs that have both X-ray and optical data, including redshifts (for recent review see, e. g., Brandt & Hasinger 2005). Hasinger, Miyaji, & Schmidt (2005) compiled a sample of  $\sim 1000$  X-ray sources with energies of 0.5–2 keV from ROSAT, Chandra, and XMM-Newton observations that were optically identified

---

<sup>1</sup>Both pointlike QSOs and resolved galaxies with active nuclei are referred to in this paper as AGNs.

<sup>2</sup>In this work we have made use of data obtained from the US National Virtual Observatory, which is sponsored by the National Science Foundation

with AGNs. With that sample they derived for the first time reliable space densities of X-ray selected AGNs at cosmological distances. They quantified in much detail previous findings on the strong luminosity-dependent cosmological evolution of these objects, confirming the density peaks at  $z \sim 2$  and  $z \lesssim 1$  near the high and low limits, respectively, of the AGN X-ray luminosity range ( $\log L_x \sim 45$  and 42).

Barger et al. (2005) looked into cosmological evolution of AGNs using a few hundred optically identified hard Chandra X-ray sources with redshifts from spectroscopy or, in the case of too faint objects, estimated from optical photometry. The study found a decrease in the AGN X-ray luminosity by an order of magnitude since redshift  $z = 1.2$ . That decrease was shown to be due to AGN downsizing rather than to declining accretion rates onto the central black holes. Another result from this study suggests that the widely discussed unification model, according to which the broad-line (Seyfert 1) and narrow-line (Seyfert 2) AGNs differ only due to the line-of-sight effects (different inclinations of the black hole accreting disk) needs to be modified by including luminosity-dependent effects.

Brand et al. (2005) used a sample of  $\sim 3000$  Chandra ACIS sources with redshifts from optical photometry to study the accretion history of active nuclei. The sources were identified with red galaxies in the Bootes area. Over the redshift range  $z = 0.3 - 0.9$  the accuracy of photometric redshifts sufficed to show that the mean X-ray luminosity increases toward higher redshifts, interpreted as evidence for a substantial decline in the nuclear accretion since the epoch  $z \sim 1$ .

A rapidly growing body of evidence suggests the existence of a connection between the starburst and AGN phenomena (e.g., Kauffmann et al. 2003; Imanishi & Wada 2004). This fact is of fundamental significance, because it implies that the same physics underlies processes leading to the central burst of star formation and the AGN phenomenon, e.g., formation of a central molecular torus feeding both the starburst and the central black hole. Both phenomena are associated with a prodigious output of X rays and thus can be studied through the properties of the galaxy X-ray emission. Deep insights into intimate details of the AGN–starburst connections, hence the aforementioned underlying physics, can be gained from a study of combined X-ray and optical properties of a large sample of galaxies. If redshifts are available, the evolution of these connections can be tracked on a cosmological timescale. Recent efforts along these lines, which are based on the Chandra X-ray Observatory data in the first place, have already brought significant results. Hornschemeier et al. (2005) cross-correlated the Chandra sources from the archive of ACIS observations with SDSS galaxies. The resulting sample of 42 galaxies with redshifts within  $z = 0.03 - 0.25$  was used to compare optical spectroscopic diagnostics of galaxy activity, both star formation and nuclear accretion. Although the small size of the sample limited the scope of issues that could be addressed with it, a number of substantial results were obtained. In particular, all X-ray-luminous, X-ray-hard galaxies were found to have AGN spectroscopic signatures. This supports earlier claims that simple observational effects may explain the puzzle of the class of X-ray–bright, optically normal galaxies (XBONGs) seen in the Chandra and XMM-Newton observations of galaxies at moderate redshifts. But the sample used is rather small, and statistically larger samples of both

normal and AGN X-ray galaxies are still needed in order to either firmly rule out or confirm high X-ray luminosities that are due to mechanisms other than an AGN.

Optical spectra and redshifts will continue to be the main challenge in achieving the full science potential of modern X-ray missions such as Chandra and XMM-Newton. This is also true for the ROSAT data, although the situation here is in some sense much better. The reason is that the ROSAT data can be supported to a much larger degree by the rich SDSS optical data. Anderson et al. (2003) emphasized that the ROSAT All Sky Survey and the SDSS survey are well matched in many respects, most importantly in terms of sensitivity. The sensitivity match is even better for the PSPC pointed observations, where a typical flux limit of  $\log f_x \sim -13.2$  samples very well the peak in the SDSS AGN brightness distribution at the AGN sample  $i$ -band limiting magnitude of  $\sim 19$  (see the  $\log f_x - i$  relationship below). Therefore, although less deep and having lower positional accuracy than the Chandra and XMM-Newton, and sampling only the soft ( $< 2.5$  keV) X-ray band, the ROSAT catalogs remain indispensable for many scientific issues of current interest. There are a few thousand ROSAT sources, mainly from the shallow All-Sky Survey, identified with resolved SDSS AGNs and/or starburst galaxies in the low-redshift Universe,  $z < 0.6$ . The number counts in the similarly soft samples of the Chandra objects at these redshifts are typically limited to less than a hundred (see, e.g., Green et al. 2004; Barger et al. 2005; Hornschemeier et al. 2005). Prior to the SDSS barely more than a thousand of ROSAT sources were identified with optically known AGNs (Brinkmann, Yuan, & Siebert 1997; Yuan, et al. 1998). The initial catalog by Anderson et al. (2003) of SDSS AGNs with X-ray emission from the RASS contains  $\sim 1200$  objects; this number was increased to 3366 by Shen et al. (2005) using SDSS DR3 AGNs.

In this paper we present a catalog of 1744 AGNs from SDSS DR4 with X-ray emission from ROSAT PSPC pointed observations, which are substantially deeper than those in the RASS. Half of these AGNs are in the low-redshift Universe,  $z < 0.6$ , similar to the AGNs in the Andersen et al. (2003) catalog. A significant fraction,  $\sim 20\%$ , are resolved SDSS objects, so their morphology can be studied from SDSS images. Statistically large samples of such AGNs will be especially useful to study AGN-starburst connections, the role of galaxy mergers in the AGN phenomenon, the relationships between the galaxy bulges and the central black holes (e.g., Heckman et al. 2004), and other problems for which the knowledge of the details of galaxy morphology is essential. The sample's usefulness for some other problems is limited, however, by selection effects present in both the WGACAT and SDSS. For instance, both the WGACAT sources and the SDSS QSO (AGN) sample are biased against obscured AGNs. Soft X-ray emission that can be detected with ROSAT is absorbed in such objects, and instruments operating in harder X-ray bands, such as Chandra and XMM-Newton, are needed to observe them. Obscuration also depresses AGN spectral features in the optical. Because of that the SDSS QSO (AGN) sample misses the population of heavily obscured AGNs. Due to these effects the catalog we present is essentially limited to Type 1 AGNs. The above selection effects are not the only ones, and in this paper we discuss more of them.

## 2. The catalog

### 2.1. The WGACAT data

In the 4 yr period of ROSAT pointed observations with the PSPC (Position Sensitive Proportional Counter),  $\sim 18\%$  of the sky was covered, more or less randomly, to various degrees of sensitivity. The WGACAT was created by reprocessing data from these observations (see, e.g., White et al. 2002 at <http://wgacat.gfsc.nasa.gov>). The exposure times were typically 100 times longer than in the 6 month ROSAT All-Sky Survey program. The source detection algorithm was optimized for point sources, although sources in which extended emission is present are also found. The catalog provides count rates in the 0.1 – 2.4 keV band and three narrow bands along with supporting information for 76,763 unique sources detected in the PSPC field of view within 60 arcmin from the detector axis. Some sources were observed repeatedly; the WGACAT contains separate entries for each individual observation, so there are a total of 88,579 catalog entries. Since both the sensitivity and positional accuracy of ROSAT PSPC decrease with increasing offset from the detector axis, we use in our studies only the data obtained at the smallest off-axis angles; if the source off-axis angles in different exposures are the same then the data from the largest exposure time is used.

Less than 15% of the sources, mostly the brightest ones, were identified in the WGACAT with stars, galaxies, AGNs, and other objects as a result of positional cross-correlation against 92 catalogs of optical, radio, X-ray, and infrared sources. The sample of identified sources was employed by McGlynn et al. (2004) to build the automated classifier ClassX that determines the likely object type for any WGACAT source. The vast majority of the previously unidentified sources were classified by ClassX as AGNs (object classes QSO and AGN in the classification scheme discussed by McGlynn et al. 2004). Many of them are expected to be X-ray counterparts of SDSS AGNs in the fields where the two surveys overlap, so optical identification for these sources can be derived from positional cross-correlation of SDSS AGNs with the WGACAT sources.

Because of the design of the ROSAT PSPC instrument and the way the ROSAT PSPC pointed observations program was carried out, the WGACAT represents a data set that is in general neither flux limited nor complete to any given flux level. One of the reasons is that the exposure times at different pointings were not the same, so the detection limit varies between different pointings. But even at the same pointing the sources detected at larger offsets from the detector axis are skewed toward higher fluxes due to decline in the detector sensitivity with increasing off-axis distance. The respective selection effects would transfer to any sample of objects with the WGACAT X-ray, impacting the sample’s statistics. Therefore, interpretation of the relationships obtained from such samples would require a careful analysis of these effects. We addressed them at some level while illustrating below the properties of the SDSS X-ray AGNs presented in this paper. However, depending on the scientific problem at hand, a deeper analysis would typically be needed.

## 2.2. Cross-correlation of SDSS DR4 AGNs with the WGACAT sources

The sample of SDSS AGNs cross-correlated with WGACAT includes all 57,800 objects from Data Release 4 (Abazajian et al. 2005) that have SDSS spectral type 3, which corresponds to AGNs, and have measured brightness in all five bands. Because of the AGN selection algorithm used in SDSS, almost all of them are Type 1 AGNs, i.e., those with broad emission lines (QSOs and Type 1 Seyfert galaxies). Following Anderson et al. (2003), positional cross-correlation of the SDSS DR4 AGNs with the WGACAT sources was performed using a search radius of 60 arcsec. The first run of the cross-correlation resulted in 1720 X-ray counterparts. Analysis of that run revealed, however, that the X-ray source coordinate offset from the respective position of the SDSS object has a systematic component as a function of the source off-axis angle  $\theta$ , which signaled the presence of a systematic error in the source coordinates in the WGACAT ( $\theta$  is the angular offset of a source position from the central axis of the PSPC field of view). Figures 1 and 2 illustrate the problem. This systematic error can be reduced, if not eliminated, by applying coordinate corrections derived from a regression analysis such as shown in Figures 1 and 2. Specifically, based on these Figures, we corrected the original X-ray source coordinates,  $RA_{\text{ori}}$  and  $Dec_{\text{ori}}$ , as follows:

$$RA = RA_{\text{ori}} - (1.372 + 0.227\theta)/3600, \quad (1)$$

$$Dec = Dec_{\text{ori}} - (2.119 - 0.260\theta)/3600. \quad (2)$$

In this way the SDSS data helped to improve the WGACAT coordinates. The second run of cross-correlation using new coordinates resulted in 1744 X-ray counterparts, 24 more than in the first run. There were only four cases in which the same WGACAT source was within the search radius of more than one SDSS AGN; in these cases the AGN closer to the X-ray source was selected. All the correlations that we studied with this new set of SDSS X-ray AGNs yielded better results, which indicates that the coordinate improvement, even though small, was real.

The reliability of the identification of the WGACAT sources with the AGNs in our sample can be directly assessed as follows. Given the footprint area of the SDSS DR4 spectroscopic sample of 4783 deg<sup>2</sup>, and assuming the WGACAT sky coverage of 18%, we get the estimated footprint area of the PSPC pointed observations  $S_{\text{xray}} = 861$  deg<sup>2</sup>. The estimated numbers of AGNs and X-ray sources in this area are  $N_i = 10396$  and  $N_{\text{xray}} = 8853$ , respectively. The ratio of the area within the cross-correlation radius to the footprint area gives an estimate of the probability for an X-ray source to turn up spuriously within the cross-correlation radius of an AGN. For the 1 arcmin radius this ratio is  $P_s \sim 10^{-6}$ . For the radius of 30 arcsec, where we find the majority of the X-ray–optical matches, 1252 of 1744 (72%), this ratio is correspondingly 4 times smaller,  $P_s \sim 2.5 \times 10^{-7}$ . So the expected number of spurious X-ray–optical associations is  $N_s = N_{\text{xray}} \times N_i \times P_s = 92$  and 23, respectively, or  $\sim 5\%$  and  $\sim 2\%$  of the actually detected matches within these two radii. The summary of the cross-correlation statistics is shown in Table 1.

The estimated percentage of spurious positional coincidences, 5% for the 60 arcsec radius, proves to be the same as in Anderson et al. (2003), where it was obtained for the RASS sources

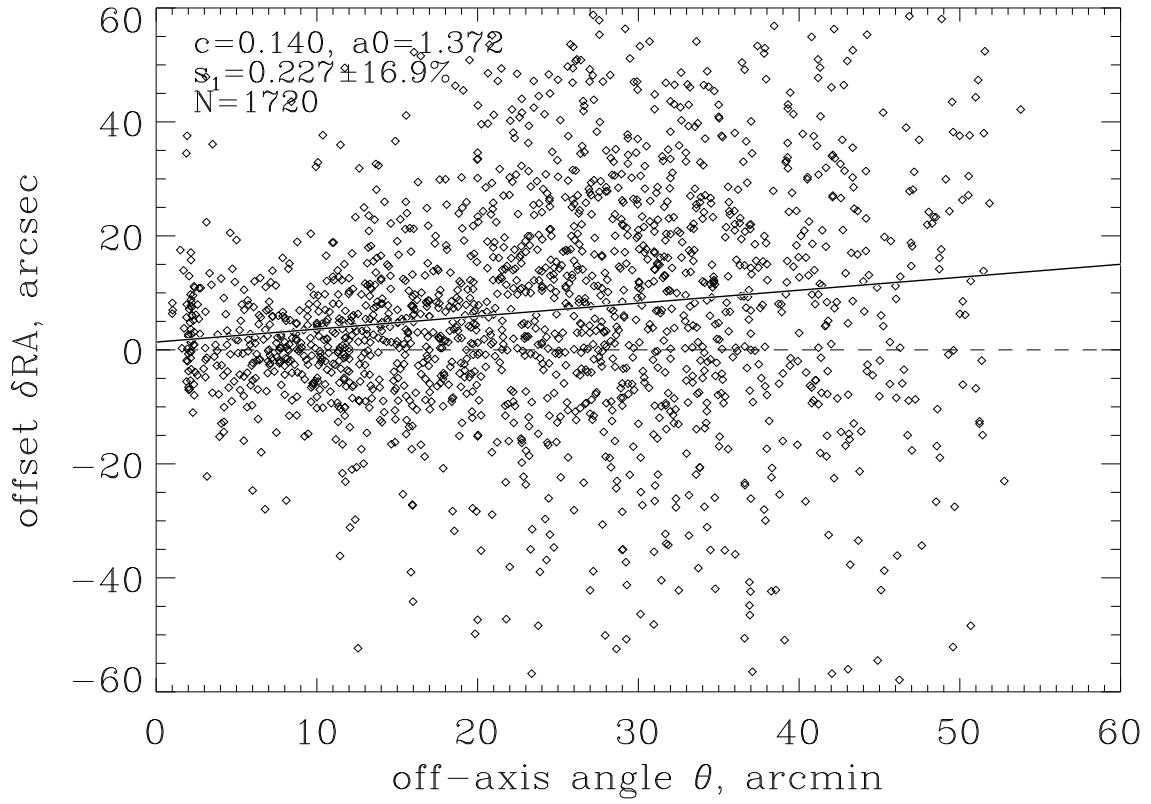


Fig. 1.— SDSS-WGACAT positional offset in right ascension,  $\delta RA$ , vs. X-ray source off-axis angle,  $\theta$ . The  $\theta$ -dependent positive bias seen in this diagram indicates the presence of a systematic coordinate error.

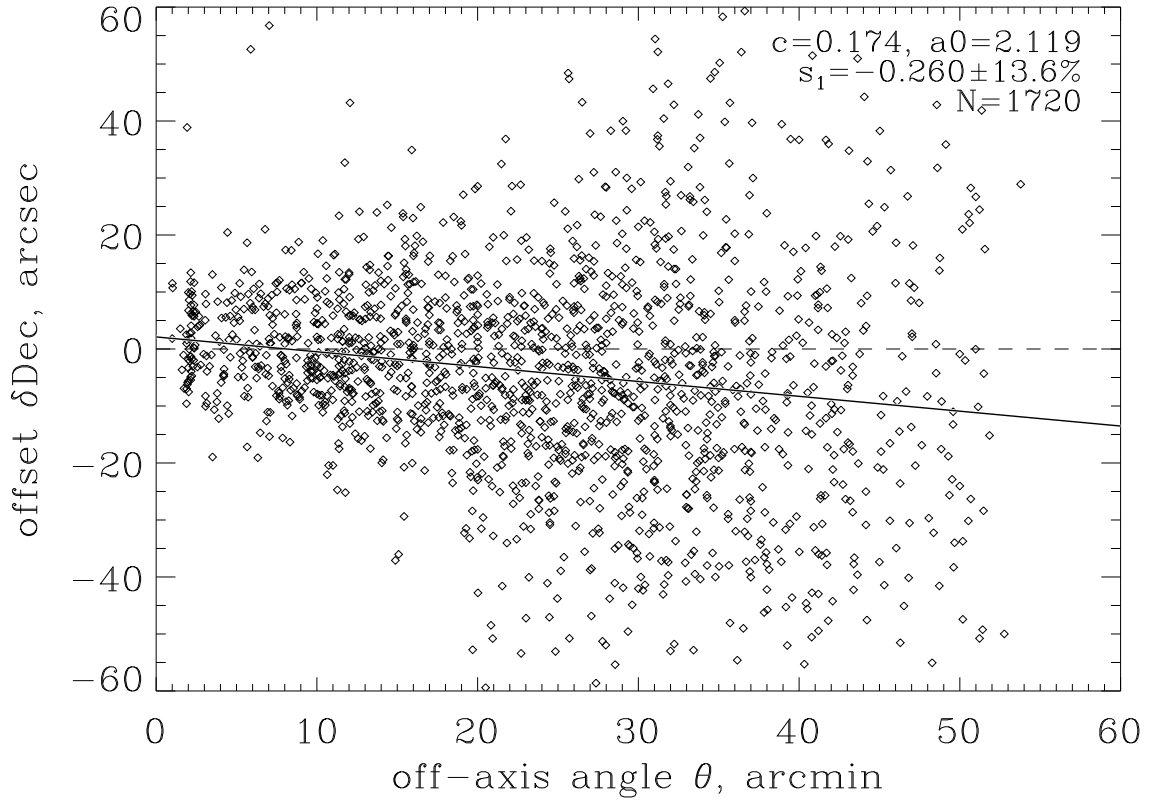


Fig. 2.— Same as Figure 1 but for positional offset in declination. An indication of a systematic source coordinate error is evidenced by the increasing negative bias in  $\delta\text{Dec}$  toward larger off-axis angles.



cross-correlated with SDSS AGNs in the 1400 deg<sup>2</sup> sky area. Another similarity between the RASS and WGACAT cross-correlation results is in the shape of the X-ray–optical positional offset distribution. Both the SDSS–WGACAT and SDSS–RASS offset distributions peak at  $\sim 10$  arcsec, (compare our Figure 3 with Figure 8 in Anderson et al. 2003). The high reliability of our SDSS–WGACAT cross-identifications is consistent with the results of classification of WGACAT sources with ClassX X-ray classifiers<sup>3</sup>. The classifier trained only on X-ray data yielded 1414 (81.1%) of sources as QSOs or AGNs; within classification uncertainties of the classifier, this is consistent with all the sources being actually AGN or QSO objects.

Of 1744 SDSS X-ray AGNs 334 (19.1%) are identified in the WGACAT with previously known QSO or AGN objects, while 1410 (80.9%) are new AGN identifications. The bulk of the AGNs, 79.4%, have redshift confidence  $P_z \geq 0.95$ . In comparison, the sample of all SDSS DR4 AGNs has only 70.6% of objects with high-confidence redshifts.

### 2.3. The catalog data

The catalog presented in this paper contains optical, X-ray, and radio parameters as shown in Table 2. The format, name, and short description of the parameters are as follows:

- 1 I4 ID : ID number
- 2 A19 SDSS ID : SDSS ID
- 3 F11.6 RA : R.A. from SDSS (J2000.0, degrees)
- 4 F11.6 Dec : Dec. from SDSS (J2000.0, degrees)
- 5 F6.3 Redshift : Redshift
- 6 F4.2  $P_z$  : Redshift confidence
- 7 I2 MT : SDSS morphology type: resolved (3) or unresolved (6)
- 8 F7.3  $u$  : Dereddened  $u$  magnitude
- 9 F7.3  $e_u$  : Error on  $u$  magnitude
- 10 F7.3  $g$  : Dereddened  $g$  magnitude
- 11 F7.3  $e_g$  : Error on  $g$  magnitude
- 12 F7.3  $r$  : Dereddened  $r$  magnitude
- 13 F7.3  $e_r$  : Error on  $r$  magnitude
- 14 F7.3  $i$  : Dereddened  $i$  magnitude
- 15 F7.3  $e_i$  : Error on  $i$  magnitude
- 16 F7.3  $z$  : Dereddened  $z$  magnitude
- 17 F7.3  $e_z$  : Error on  $z$  magnitude
- 18 A18 WGACAT ID : WGACAT ID
- 19 I4  $\delta r$  : Offset of the X-ray source from the SDSS position (arcsec)
- 20 I4  $\theta$  : X-ray source offset from the PSPC axis (off-axis angle, arcmin)
- 21 F8.4  $C_{0.1-2.4}$  : Count rate in the broadband, 0.1 – 2.4 keV
- 22 F8.4  $e_{C_{0.1-2.4}}$  : Error on the broadband count rate
- 23 F8.4  $\log f_x$  : Logarithm of broadband X-ray flux corrected for Galactic absorption ( ergs cm<sup>-2</sup> s<sup>-1</sup>)
- 24 F8.4  $\log L_x$  : Logarithm of broadband X-ray luminosity corrected for Galactic absorption ( ergs s<sup>-1</sup>)
- 25 F8.4 HR1 : Hardness ratio 1 (corrected for Galactic absorption)
- 26 F8.4 HR2 : Hardness ratio 2 (no Galactic absorption correction applied)
- 27 F8.4 FIRST ID : FIRST ID

---

<sup>3</sup><http://heasarc.gsfc.nasa.gov/classx>

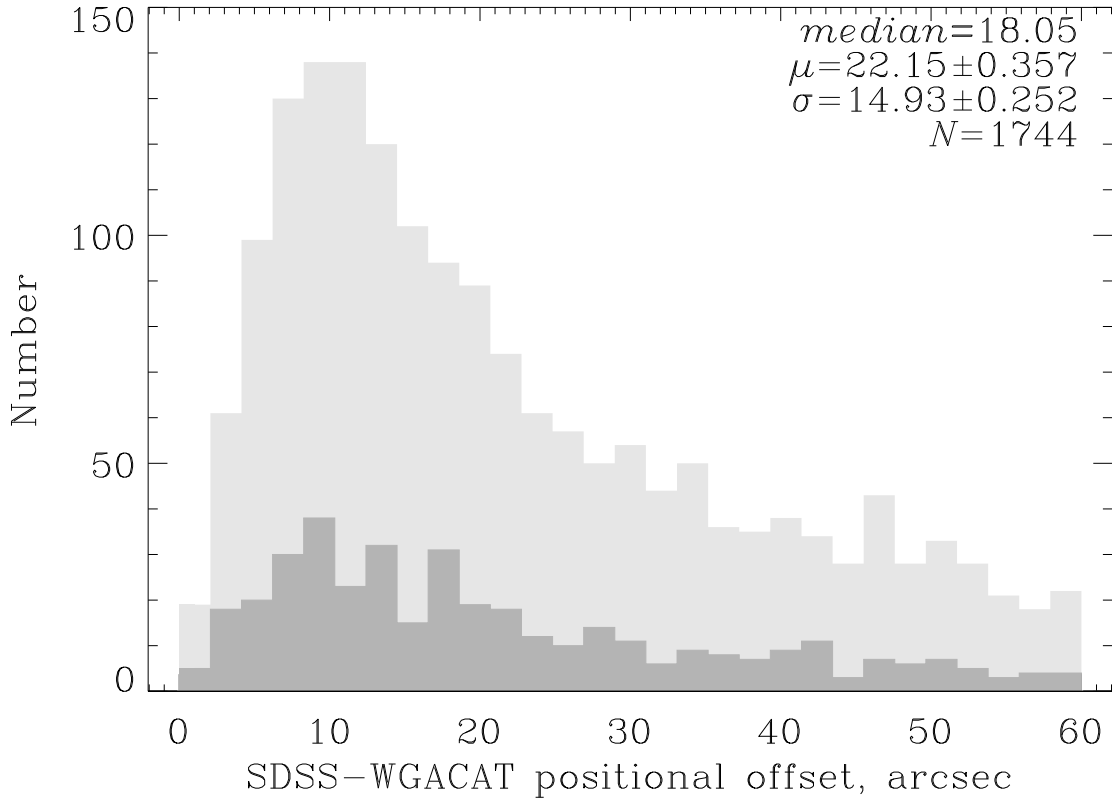


Fig. 3.— Distribution of the SDSS-WGACAT positional offsets. The legend in this and similar figures gives the histogram mean,  $\mu$ , standard deviation,  $\sigma$ , and the median; dark shading indicates resolved AGNs only. The distribution is very similar to that obtained by Anderson et al. (2003) for the SDSS-RASS positional offsets, which was argued to be as expected if the respective SDSS AGNs were statistically proper identifications of ROSAT sources.

- 28 F8.4  $f_{\text{peak}}$  : Logarithm of the peak 1.4 GHz flux (mJy)
- 29 F8.2  $f_{\text{int}}$  : Logarithm of the integrated 1.4 GHz flux (mJy)
- 30 F8.2 rms : Flux rms
- 31 F8.2  $\log L_{1.4\text{GHzpeak}}$  : Logarithm of the peak 1.4 GHz luminosity ( ergs s<sup>-1</sup>Hz<sup>-1</sup>)
- 32 F8.2  $\log L_{1.4\text{GHzint}}$  : Logarithm of the integrated 1.4 GHz luminosity ( ergs s<sup>-1</sup>Hz<sup>-1</sup>)

The SDSS parameters include dereddened SDSS magnitudes,  $u, g, r, i,$  and  $z$ , magnitude errors, redshift, and redshift confidence (although we denote both redshift and  $z$ -band magnitude as  $z$ , the meaning of  $z$  is always clear from the context). Also included are SDSS coordinates, RA and Dec, and SDSS morphological type, which in our case is either 3 (resolved objects) or 6 (unresolved objects).

The X-ray parameters include the positional offset between the SDSS and ROSAT sources,  $\delta r = [(\delta \text{RA})^2 + (\delta \text{Dec})^2]^{1/2}$ , X-ray source off-axis angle,  $\theta$  (source angular distance from the PSPC axis), and broadband (0.1 – 0.4 keV) count rate corrected for vignetting and PSF variation across the PSPC field. Derived parameters include broadband X-ray flux,  $f_x$ , and X-ray luminosity,  $L_x$ , corrected for galactic absorption. These two parameters were computed using photon index  $\Gamma = 2$  (see, e.g., Brinkmann et al. 1997; 2000). The cosmology adopted in this paper is  $H_0 = 70 \text{ km s}^{-1} \text{ Mpc}^{-1}$ ,  $\Omega = 0.3$ , and  $\Lambda = 0.7$ .

As seen in Figure 4, at low energies, 0.1 – 0.4 keV (soft band), absorption by the Galactic neutral hydrogen can be quite significant for our sources. But no absorption is evident at 0.4 – 0.9 (mid band) and 0.9 – 2.4 keV (hard band) for the range of HI column densities shown in Figure 4. The column density of the absorbing material,  $N_{\text{HI}}$ , shown in Figure 4 was computed based on the Dickey & Lockman (1990) and Stark et al. (1992) data. Absorption effects in the soft-band count rate can be accounted for on a purely empirical basis by removing the trend revealed by Figure 4:

$$\log C_{\text{soft}} = \log C_{\text{soft}}^{\text{absorb}} + s_1(19.8 - \log N_{\text{HI}}), \quad (3)$$

where  $s_1 = -0.815$ . Equation (3) assumes that soft-band absorption becomes negligible at  $\log N_{\text{HI}} < 19.8 \text{ cm}^{-2}$ , so the latter value was used for normalization in Equation (3). The parameter  $C_{\text{soft}}$  from this equation is used to compute the hardness ratio HR1. The catalog includes two hardness ratios, HR1 and HR2, which are defined as follows:

$$\text{HR1} = \frac{C_{\text{mid}} - C_{\text{soft}}}{C_{\text{mid}} + C_{\text{soft}}} \quad (4)$$

and

$$\text{HR2} = \frac{C_{\text{hard}} - C_{\text{mid}}}{C_{\text{hard}} + C_{\text{mid}}}. \quad (5)$$

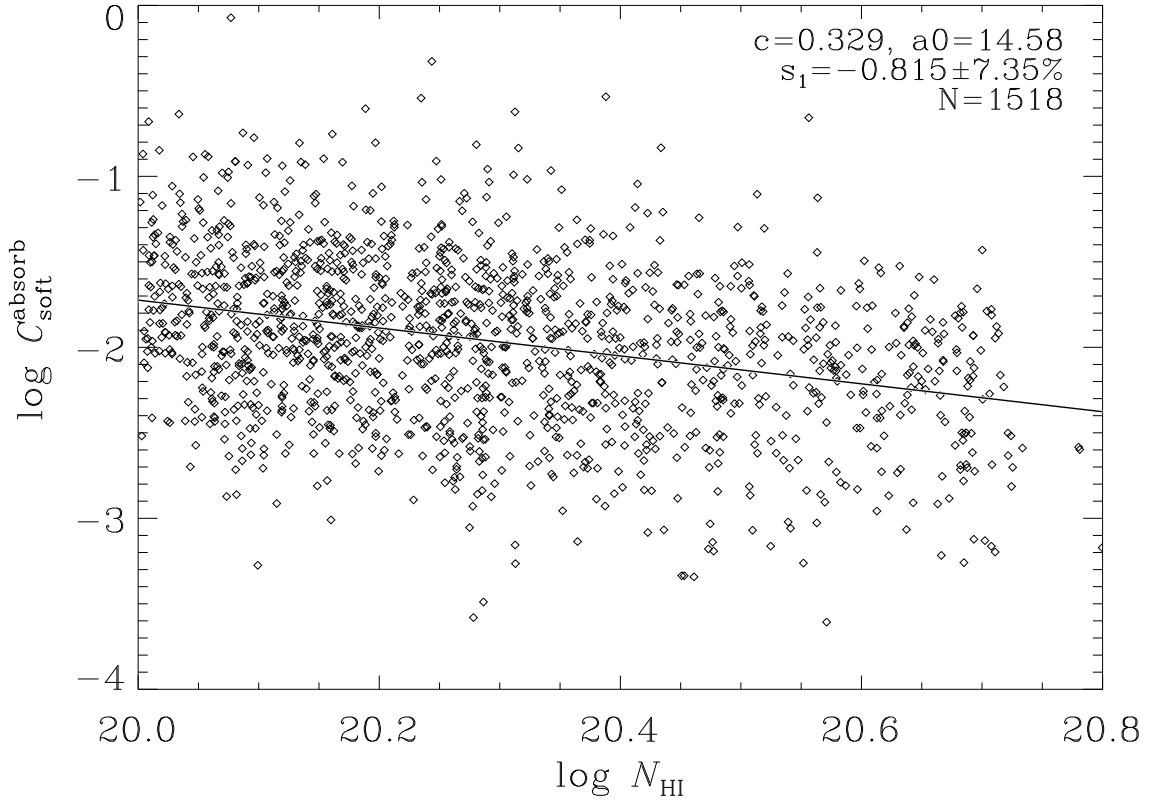


Fig. 4.— Soft-band count rate vs. Galactic HI column density. The legend in this and similar figures gives the linear regression parameters: correlation coefficient,  $c$ , intercept,  $a_0$ , and slope,  $s_1$ , with uncertainty in the slope value given in percent. The downward trend in this diagram reflects the varying Galactic absorption, implying an increase in the absorption by an order of magnitude as  $\log N_{\text{HI}}$  increases from 20 to 21  $\text{cm}^{-2}$ .

### 3. Statistics of the SDSS X-ray AGNs

#### 3.1. X-ray detection rate and optical brightness

The bulk of the SDSS DR4 AGNs are from a sample that is limited in the  $i$  band to  $i < 19.1$ . Therefore, one may expect that, similar to the  $i$ -brightness distribution of the entire SDSS AGN sample, the number of X-ray AGNs would increase toward fainter  $i$  and then sharply drop at the limiting magnitude. The actual shape of the brightness distribution depends on the detectable flux level in the ROSAT PSPC pointed observations for AGNs of various optical brightnesses. The X-ray AGN detection rate as a function of optical brightness is illustrated in Figure 5. It shows the number ratio of the AGNs detected in the X-ray and all AGNs in the sky footprint area of the PSPC pointed observations. As expected, the rate of X-ray detections is very high for bright AGNs, up to 50% and more at magnitudes  $i < 16$ . It declines to  $\sim 10\%$  at the limiting magnitude of the SDSS main quasar sample,  $i = 19.1$ . Despite this decline, the brightness distribution of the X-ray AGNs in our sample sharply increases toward the limiting magnitude (Figure 6), which is obviously due to an even sharper increase in the number of SDSS AGNs toward faint magnitudes. The distribution is nearly flat within  $i \sim 19 - 20$ , where AGNs from outside of the SDSS AGN main sample dominate. This implies that a large number of X-ray sources matching yet-unidentified AGNs with  $i > 19.1$  in the SDSS photometric database should be present in the WGACAT. As indicated below, these are expected to be mostly weak sources, below the detection limit of the ROSAT All Sky Survey.

#### 3.2. Redshift distribution

Figure 7 displays the redshift distribution of the SDSS X-ray AGNs. Similar to the Anderson et al. (2003) results, the overall distribution peaks at  $z \sim 0.3$ , gradually declining to almost zero at  $z \sim 2.5$ . This is very different from the distribution of all SDSS AGNs (Figure 8), which peaks at  $z \sim 1.7$  and then sharply declines toward  $z \sim 2.5$ . This difference has to do with the evolution of the X-ray luminosity function, the depth of the WGACAT, and the fact that the spectrum in the X-ray is steeper than in the optical, with the value of the energy index typically ranging within  $\alpha_x = -1.0$  to  $-1.5$  for the power-law spectrum vs.  $\alpha_o \sim -0.5$  for the optical power-law spectrum (see, e.g., Brinkmann et al. 2000; Anderson et al. 2003).

Most of the resolved AGNs are within the redshift range  $z = 0 - 0.3$ , and their distribution peaks at  $z \sim 0.2$ . The distribution of resolved AGNs in Figure 8 is similar to that in Figure 7.

#### 3.3. X-ray flux and optical brightness

PSPC pointed observation exposures are, on average, substantially deeper than those in the ROSAT All-Sky Survey, so the WGACAT contains many sources below the RASS detection limit.

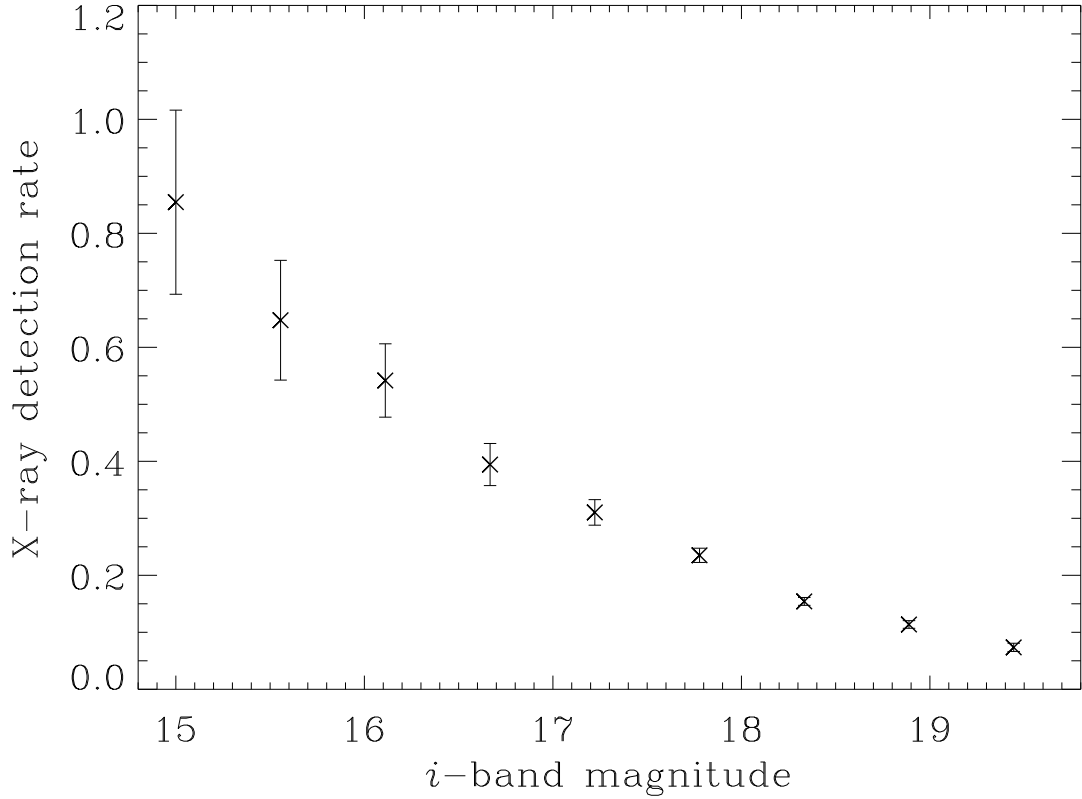


Fig. 5.— Fraction of AGNs detected in the X-ray as a function of brightness in the *i*-band. At bright magnitudes,  $i < 16$ , more than half of the SDSS AGNs in the footprint area of the ROSAT PSPC pointings are detected in the X-ray at typical exposure times of ROSAT PSPC pointed observations. This fraction drops below 20% near the brightness limit of the SDSS main quasar sample,  $i = 19.1$ .

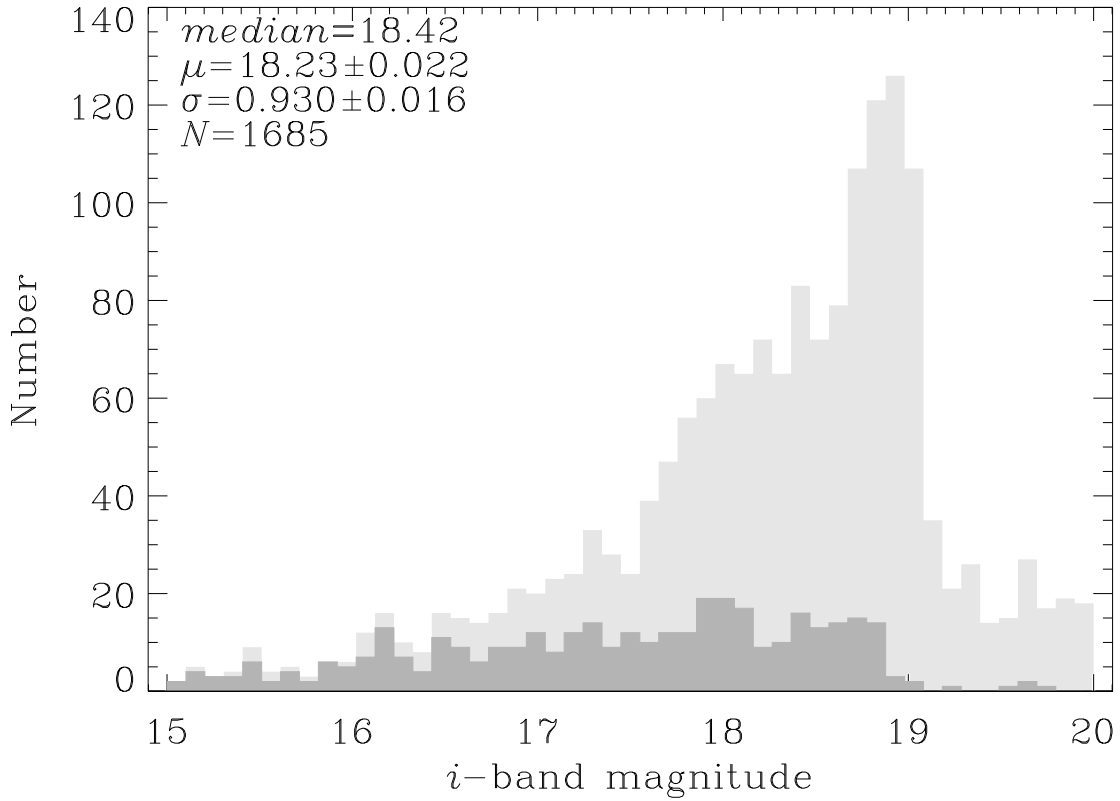


Fig. 6.— Brightness distribution of SDSS X-ray AGNs in the  $i$  band. The distribution gradually increases to the peak near the brightness limit of the SDSS AGN main sample,  $i \approx 19$ , and then sharply drops. It is nearly flat within  $i \sim 19 - 20$ , where AGNs from outside of the SDSS AGN main sample dominate. So the WGACAT should contain a large number of sources matching yet unidentified AGNs with  $i > 19.1$  in the SDSS photometric database.

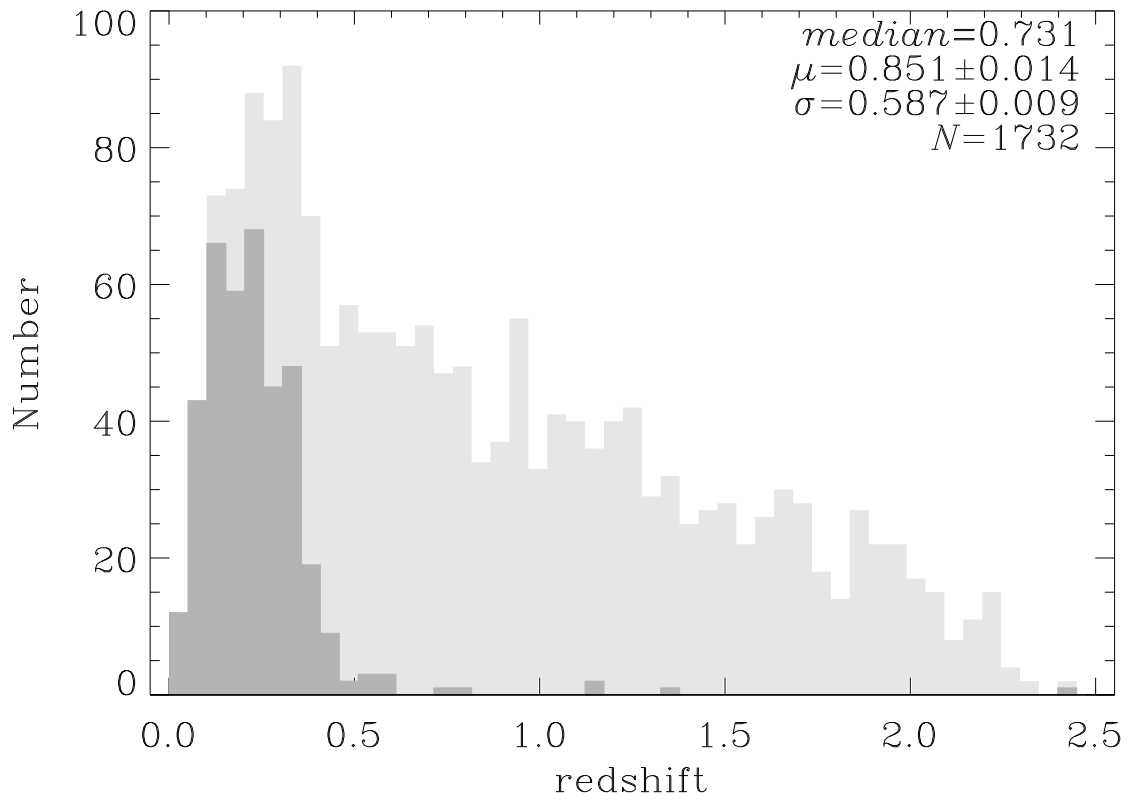


Fig. 7.— Redshift distribution of SDSS X-ray AGNs within the redshift range  $z = 0 - 2.5$  with X-ray emission from the WGACAT.



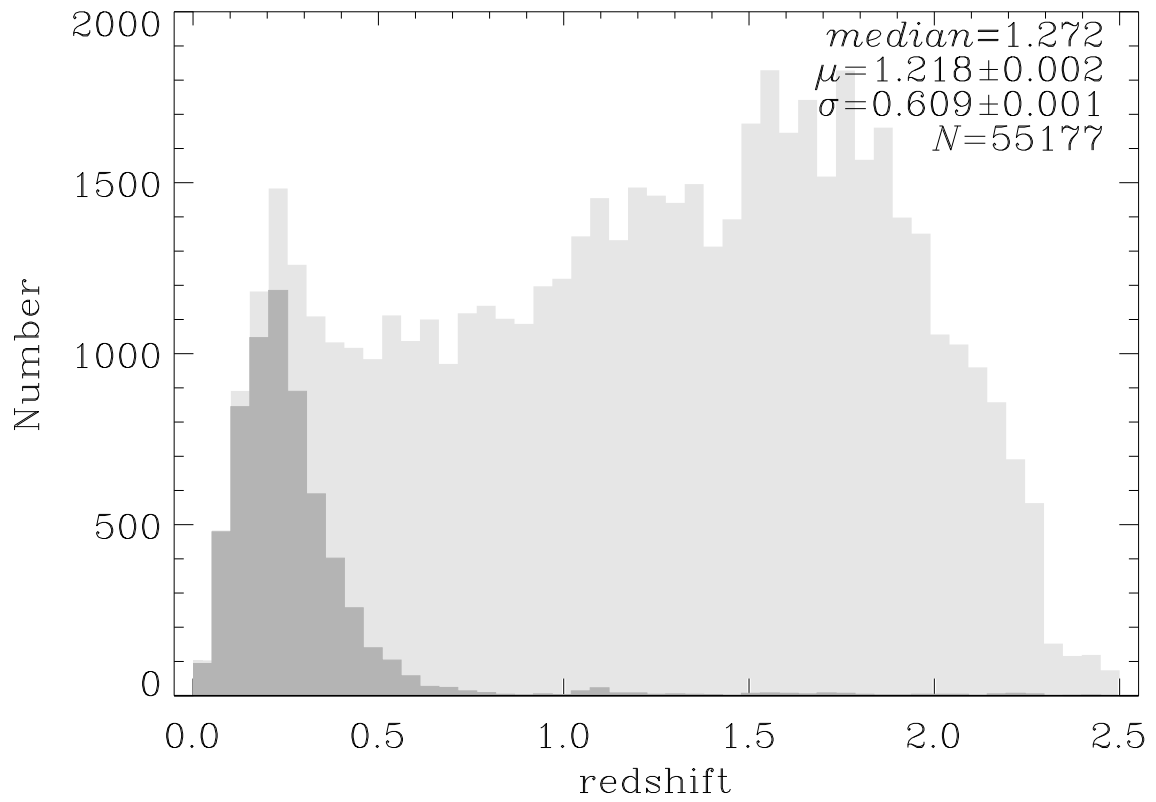


Fig. 8.— Redshift distribution of all SDSS DR4 AGNs within redshift the range  $z = 0 - 2.5$ .

Comparison of our Figure 9 with Figure 3 in Shen et al. (2005) illustrates this. While in the sample with the RASS counterparts less than 1% of the AGNs are fainter than  $\log f_x = -13$ , these are over 25% in our sample. As seen in Figure 10, they become dominant at redshifts  $z \gtrsim 1.5$ . So these low-flux objects provide an important probe for the AGN X-ray emission at redshifts  $z > 1.5$ . Among the resolved AGNs the fraction of weak X-ray sources is small (see Figure 11), consistent with a similarly low fraction of weak unresolved AGNs at low redshifts.

Figure 12 reveals a strong correlation between X-ray flux and optical brightness, which is consistent with previous studies. The sparse but uniformly distributed population in the area at the faint end of the diagram,  $i = 19 - 20$ , suggests that many more SDSS AGNs with  $\log f_x$  from  $-13.0$  to  $-13.5$  can be found among the WGACAT sources 1.0–1.5 mag fainter than the 19.1 mag brightness limit of the SDSS main AGN/QSO sample. Given that only  $\sim 20\%$  of the X-ray sources are identified with AGNs in the SDSS–WGACAT footprint area (1744 of 8853 sources), the number of X-ray AGNs fainter than  $i = 19.1$  can be a factor of 5 larger than our present sample. So our current sample can be substantially expanded in the low-flux, high-redshift domain ( $\log f_x < -13$ ,  $z > 1.5$ ) by going 1.0–1.5 mag fainter in the  $i$  band. We plan to do that in the future, using the ClassX technique (Suchkov, Hanisch, and Margon 2005) to identify these faint AGNs in the SDSS photometric database and estimate their redshift.

### 3.4. Hardness ratio

The relationship between hardness ratio and flux can provide useful information regarding X-ray absorption (see, e.g., Green et al. 2004).

The diagrams in Figures 13 and 14 present the hardness ratio for our sample plotted against the soft-band flux. In this band, 0.1 – 0.4 keV, both the resolved and unresolved AGNs exhibit essentially the same tendency to have a hardness ratio that is somewhat higher toward weaker sources. But at higher energies, in the 0.4–0.9 and 0.9–2.4 keV bands, the hardness ratio shows no trend whatsoever. This is consistent with Kim et al. (2004b) and Green et al. (2004), who concluded that spectral hardening toward faint fluxes is substantial only in the soft bands and is thus most likely due to absorption.

### 3.5. X-ray-to-optical flux ratio

Figures 15 and 16 show the X-ray-to-optical flux ratio as dependent on redshift. Resolved and unresolved AGNs exhibit opposite behavior with respect to how the X-ray-to-optical flux ratio varies with redshift. Consistent with previous studies, Figure 15 shows  $\log(f_x/f_i)$  trending down, so that the flux ratio decreases on average by a factor of  $\sim 3$  over the redshift range  $z = 0-2$ . In contrast, for the resolved AGNs, on a much smaller redshift scale, this ratio increases rather than decreases with redshift. The ratio becomes on average larger by a factor of  $\sim 3$  as redshift increases

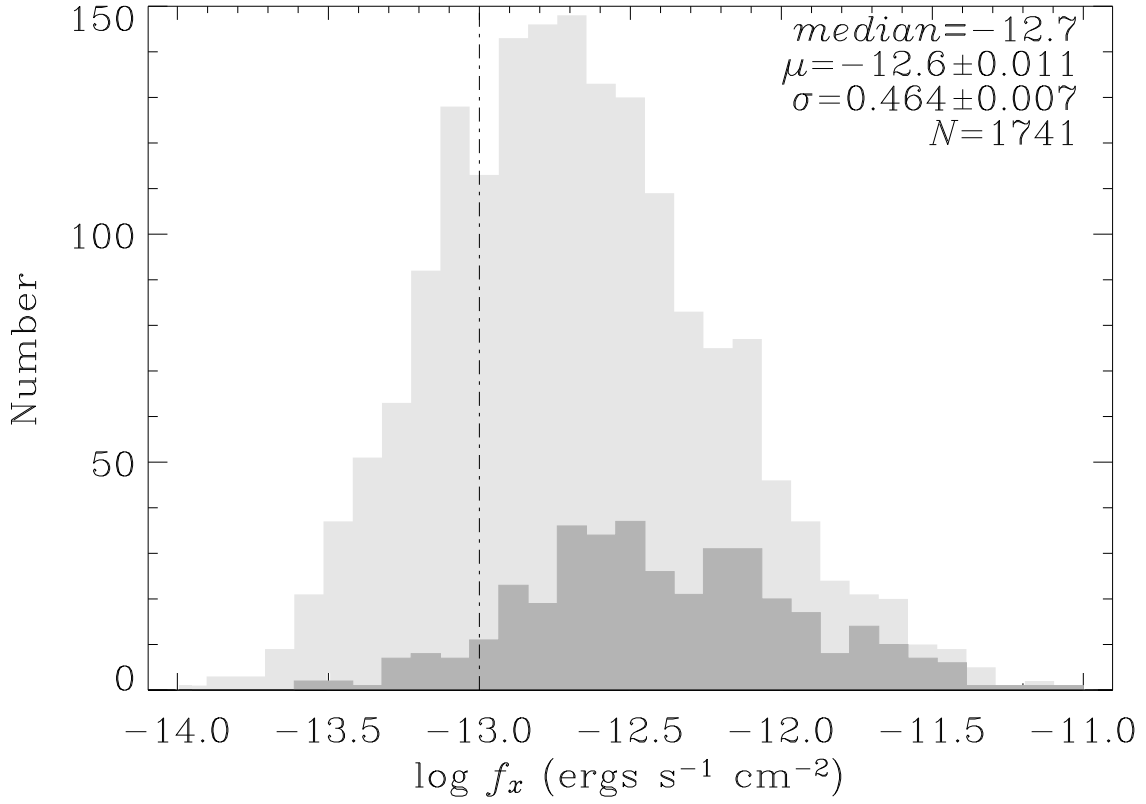


Fig. 9.— X-ray flux distribution for the SDSS-WGACAT sample. The sample is substantially deeper than the sample of SDSS AGNs with the RASS X-ray counterparts. While in the latter sample  $< 1\%$  of the sources are weaker than  $\log f_x = -13$ , these are  $\sim 25\%$  in our SDSS-WGACAT sample.

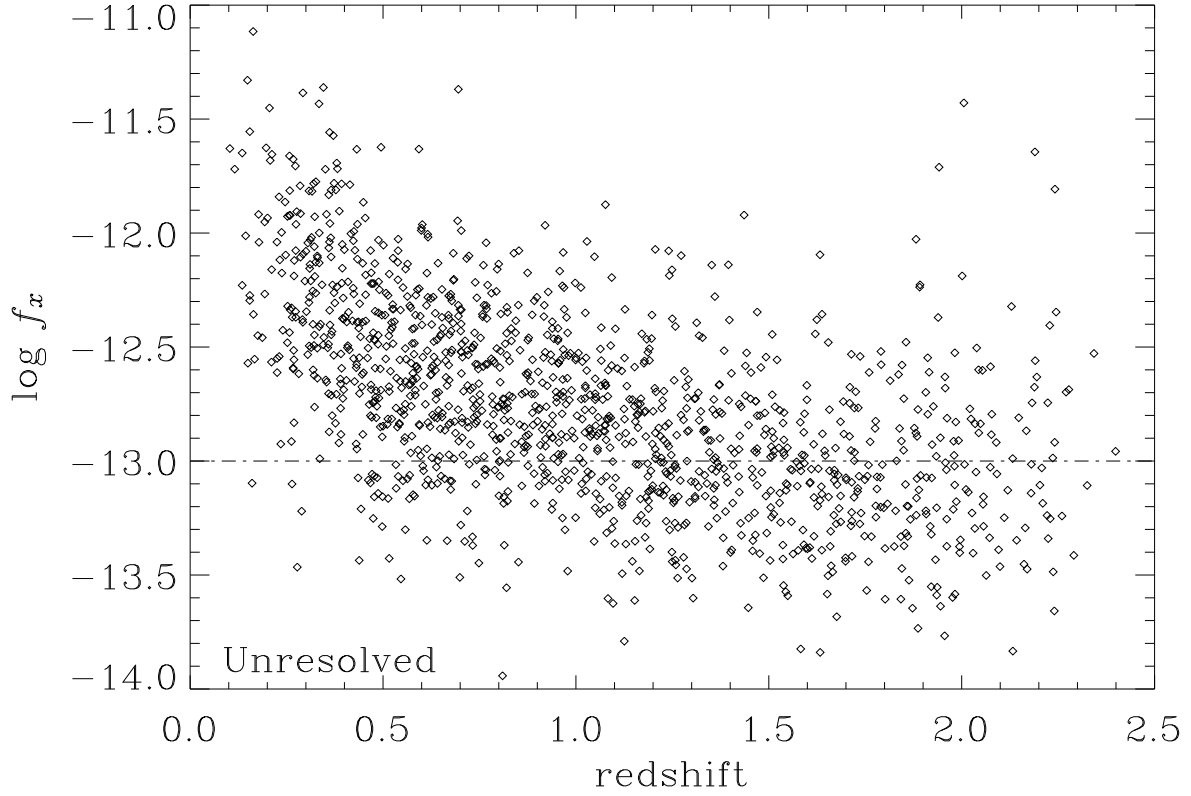


Fig. 10.— X-ray flux as a function of redshift for unresolved AGNs with redshifts  $0 < z < 2.5$ . As expected, high-redshift AGNs are weaker in the X-ray, with flux declining on average by an order of magnitude within this redshift range. Weak sources,  $\log f_x < -13$ , become dominant at  $z > 1.5$ .

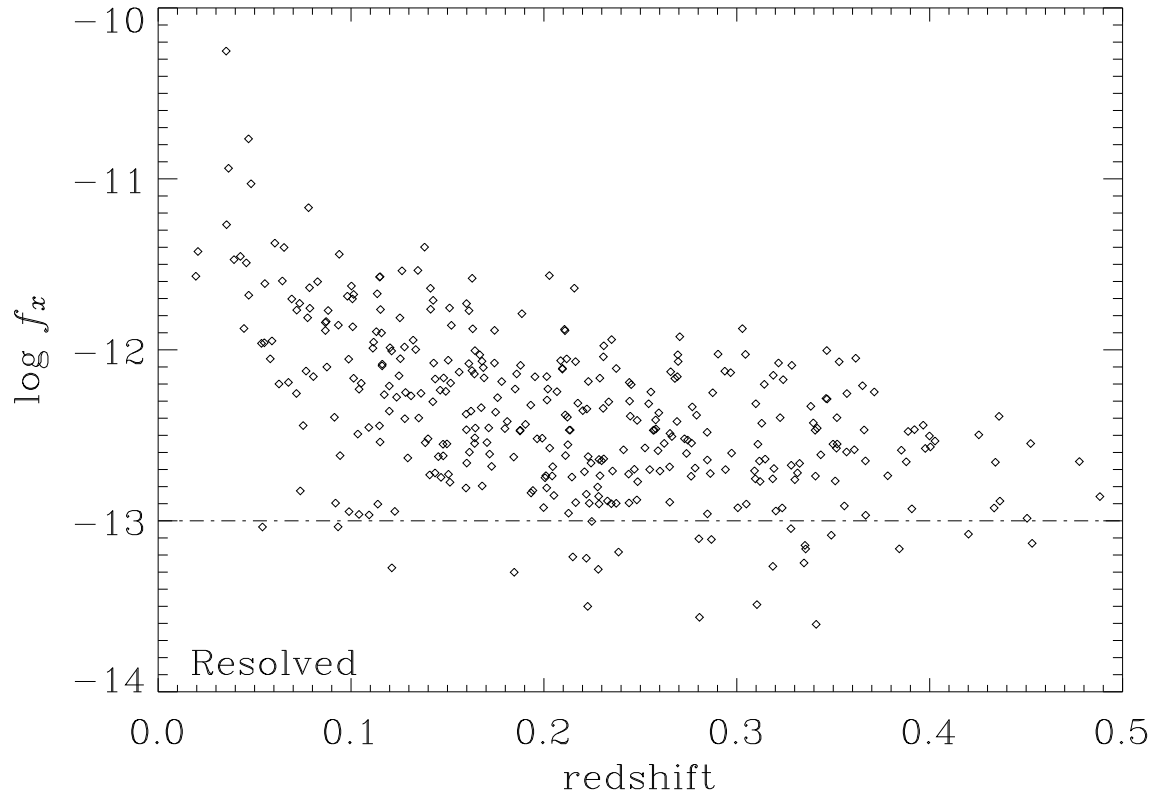


Fig. 11.— Same as Figure 10, but for resolved AGNs only and a narrower redshift range,  $z = 0-0.5$ . X-ray flux drops on average by an order of magnitude within this range.

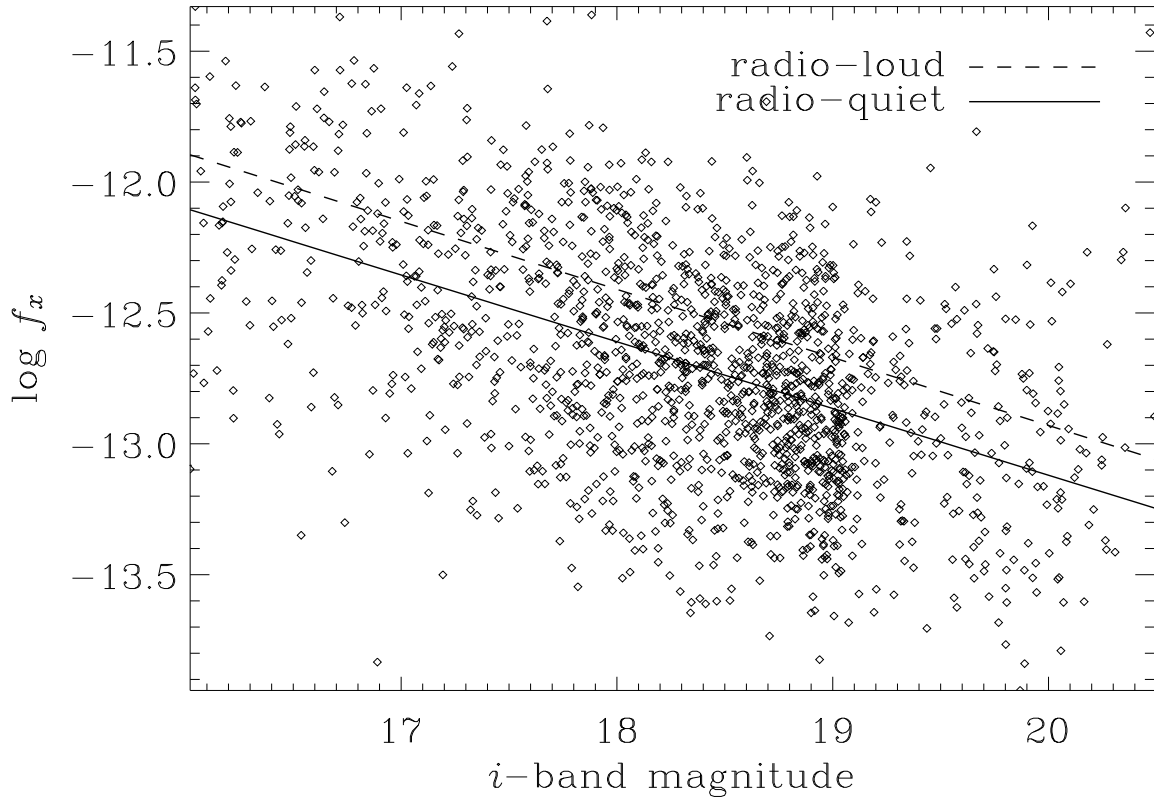


Fig. 12.— X-ray flux vs.  $i$ -band magnitude for AGNs brighter than  $i = 16$  mag. The diagram reveals the expected correlation between the two parameters (linear regression is displayed separately for radio-loud and radio-quiet AGNs) and shows that at any given brightness the radio-loud AGNs have fluxes higher than those of the radio-quiet AGNs, on average by a factor of  $\sim 2$ . It also suggests that a large number of additional WGACAT counterparts can be found for SDSS AGNs below the brightness limit of the SDSS main spectroscopic sample,  $i = 19.1$  mag.

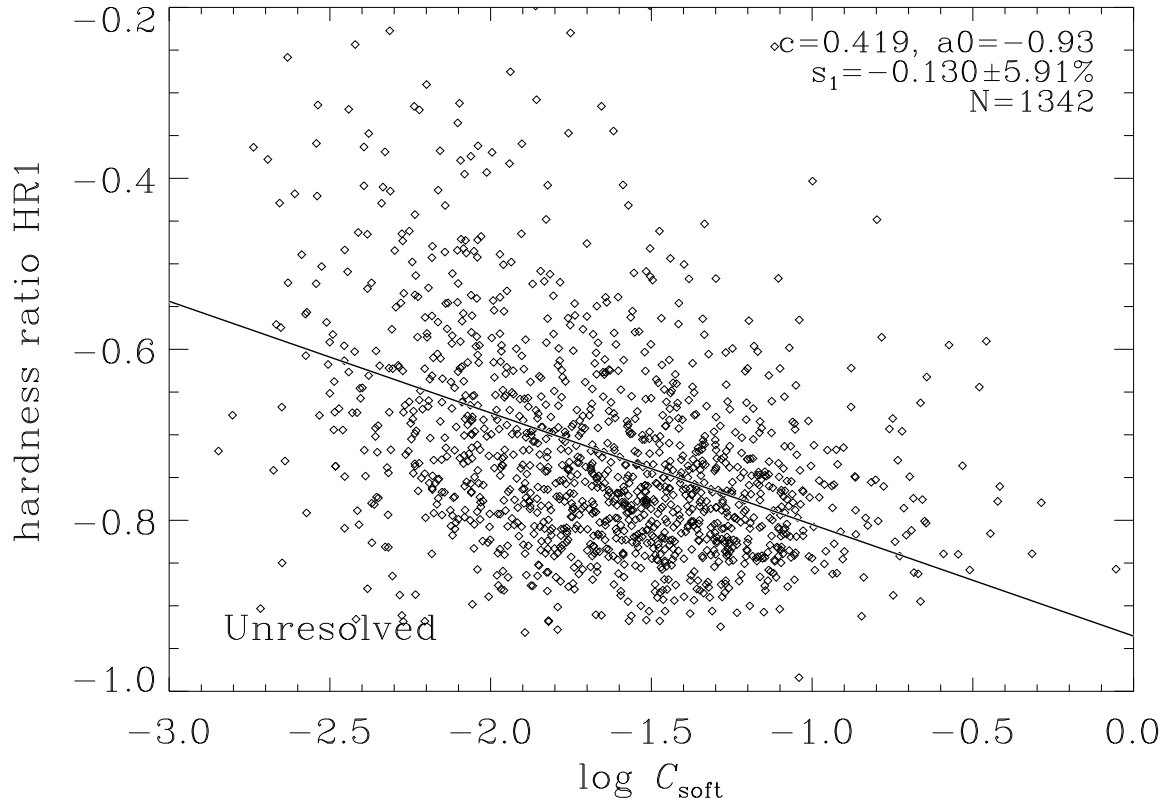


Fig. 13.— Hardness ratio HR1 vs. the 0.1 – 0.4 Kev count rate corrected for Galactic absorption. There is a tendency for hardness ratio to be higher for fainter sources, which is likely due to a larger, on average, absorption in the case of faint sources. Almost all these sources are from the area on the PSPC detector close to the detector axis,  $\theta < 20$  arcmin, where the detector sensitivity is highest.

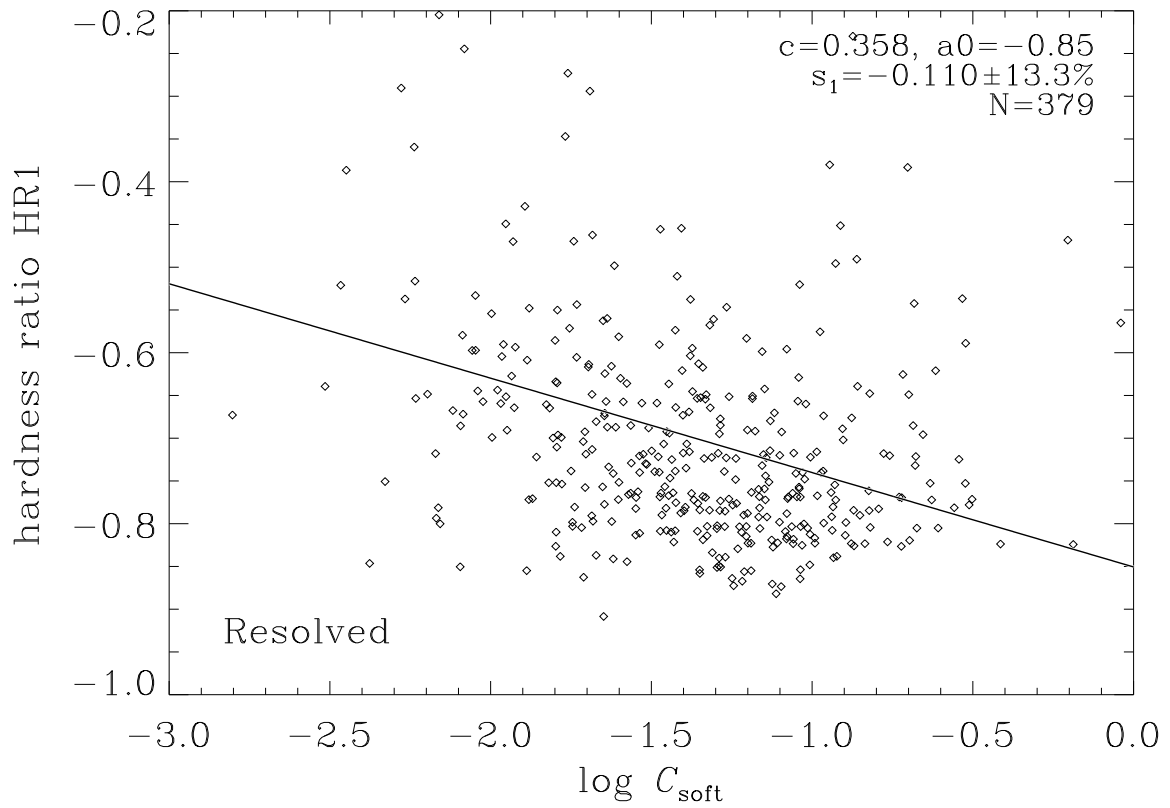


Fig. 14.— Same as Figure 13, but for resolved AGNs. Resolved AGNs exhibit essentially the same behavior as the unresolved AGNs.



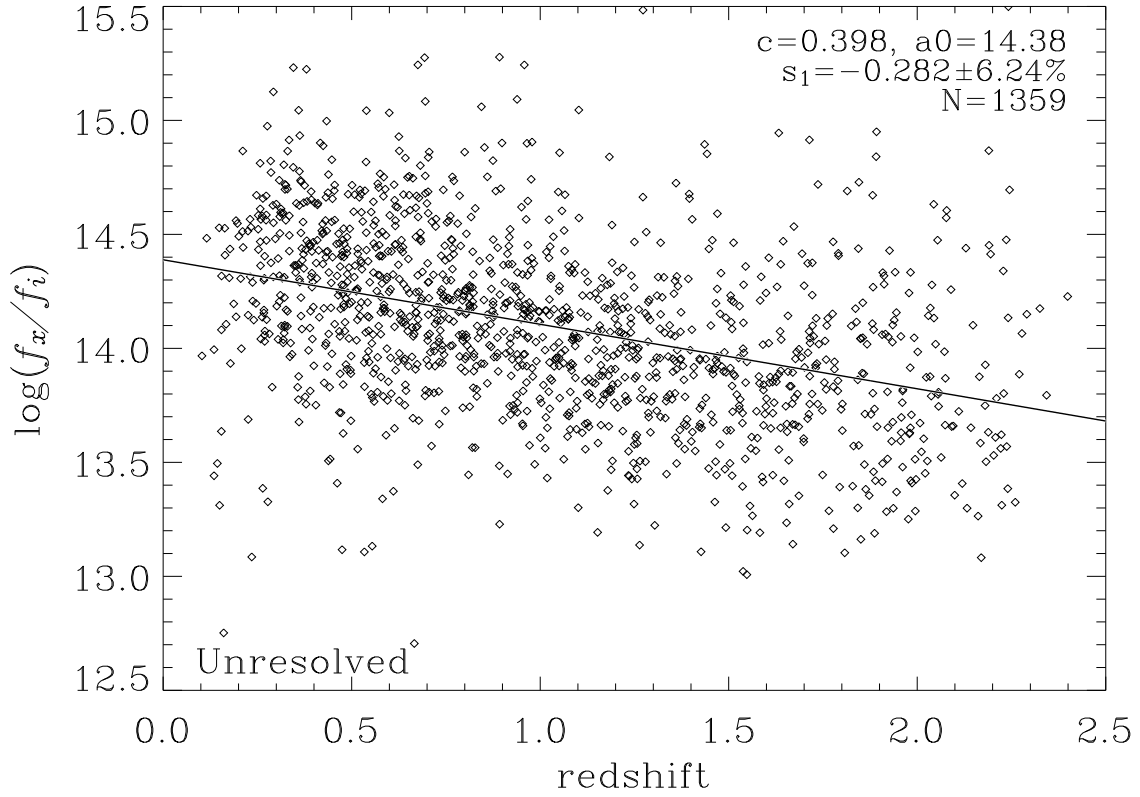


Fig. 15.— X-ray-to-optical flux ratio for unresolvable AGNs.  $f_x$  ( $\text{ergs s}^{-1} \text{cm}^{-2}$ ) is the X-ray broad-band flux, 0.1 – 2.4 keV, and  $f_i$  is spectral energy flux density in the  $i$  band ( $\text{ergs s}^{-1} \text{cm}^{-2} \text{Hz}^{-1}$ ),  $\log f_i = -0.4(i + 48.6)$ . The diagram shows the known decline of the ratio with redshift.

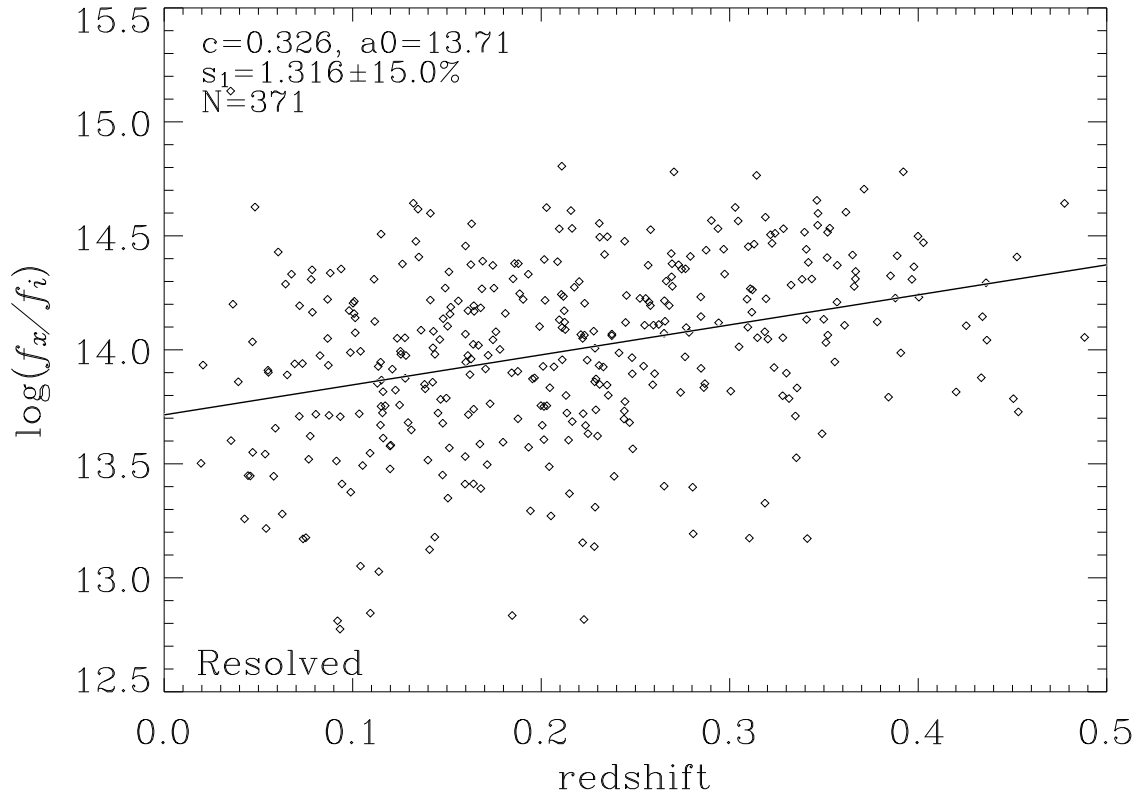


Fig. 16.— Same as Figure 15, but for resolved AGNs. In contrast with unresolved AGNs, the X-ray-to-optical flux ratio of resolved AGNs exhibits a substantial upward trend.

from 0 to 0.4 (unresolved AGNs exhibit no trend whatsoever within this narrow redshift range). This difference should be due to the fact that the optical luminosity of low-redshift active galaxies, which is dominated by stellar light, occupies a much narrower range than X-ray luminosity. Toward higher redshifts, X-ray flux can be detected only from galaxies with the highest X-ray luminosities, but optical luminosities will not be much different from those at low redshifts. As a result, the average X-ray-to-optical flux ratio gets higher. It is worthwhile to note that the flux ratio of the resolved AGNs is substantially smaller than that of the unresolved AGNs within the same range, by a factor of  $\sim 3$ .

### 3.6. Radio sources

Confronting AGN radio properties with those in the optical and X-ray can provide important insights into the diversity of AGNs. Best et al. (2005a,b) analyzed a large sample of radio-loud SDSS Type 2 AGN galaxies at redshifts  $0.03 < z < 0.3$ , which was constructed using the NRAO VLA Sky Survey (NVSS; Condon et al. 1998) and the Faint Images of the Radio Sky at Twenty cm survey (FIRST; Becker et al. 1995). They concluded that the optical and low radio-luminosity AGN phenomena are independent and are triggered by different physical mechanisms. The data suggested that while the integrated [OIII] luminosity density from emission-line AGNs is produced mainly by black holes with masses below  $10^8 M_{\odot}$ , the integrated radio luminosity density comes from the most massive black holes in the Universe. X-ray emission is another manifestation of active galactic nuclei, independent of the optical and the radio. Therefore, one may expect that combining X-ray data with radio and optical data would result in further insights into the differences between various AGNs.

Brinkmann et al. (2000) cross-correlated the ROSAT All-Sky Survey with the FIRST sources. This resulted in a sample of 843 sources, of which slightly over 100 sources were identified as various types of AGNs. But many of the X-ray–radio matches proved to be very faint in the optical. Because of the lack of spectra, and hence redshifts, these faint objects remained unclassified, which substantially impacted the scope of analysis of ROSAT radio-loud AGNs in that paper.

In this paper we also address the issue of AGN radio emission and include in our catalog the data for the AGNs for which we found radio counterparts in the FIRST catalog (the FIRST catalog can be found at <http://sundog.stsci.edu/first/catalogs.html>; see also White et al. 1997.) As Best et al. (2005a) showed, most of the FIRST sources with a 10 arcsec separation from SDSS AGNs are reliable radio identifications. So we cross-correlated 57,800 SDSS DR4 Type 1 AGNs with the FIRST sources and found 4,792 AGNs (8.3%) that have a matching radio source within 10 arcsec. We will refer to them as “radio-loud AGNs”. The FIRST sources are limited to fluxes  $\gtrsim 1$  mJy, so discrimination between our radio-loud and radio-quiet samples occurs at the flux level of  $\sim 1$  mJy.

Among the identified radio-loud AGNs, 224 objects were in our list of AGNs with X-ray emission from the WGACAT. The fraction of radio-loud AGNs in our sample, 12.8%, is thus

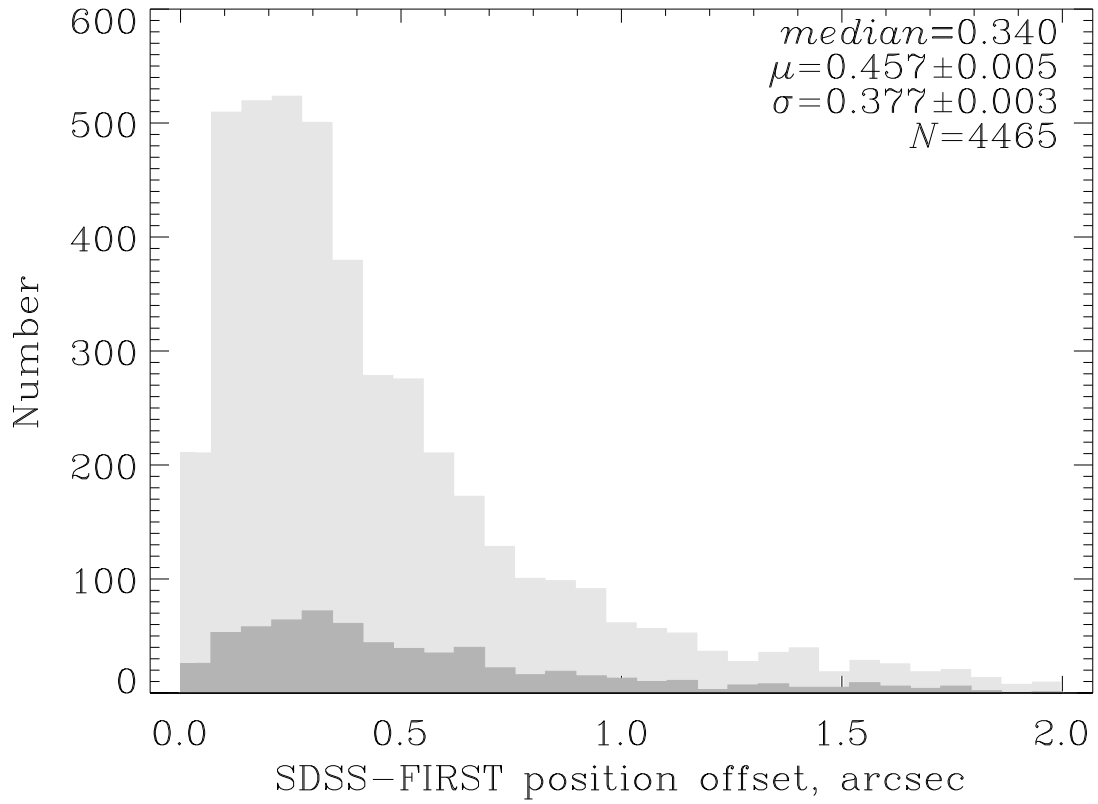


Fig. 17.— SDSS–FIRST positional offset distribution. Of a total of 4792 FIRST sources matching the position of SDSS DR4 AGNs, 4465 ( $\sim 93.2\%$ ) sources are within 2 arcsec of the SDSS AGN position.

noticeably larger than the average for SDSS AGNs, by a factor of  $\sim 1.5\%$ .

As seen in Figure 17, positional offsets of the FIRST counterparts are in general very small, with  $\sim 93\%$  of them within 2 arcsec of the SDSS position. The discrepancy between the SDSS and FIRST positions within this radius is, on average, larger for sources with larger integrated-to-peak flux ratio. This suggests that much of it is due to extended sources, for which peak radio emission does not necessarily coincide with the central optical object and source coordinates in general are less certain.

Consistent with earlier work, the X-ray emission of the radio-loud AGNs in our sample is stronger than that of the radio-quiet AGNs, on average by a factor of  $\sim 2$  at any given optical brightness (see Figure 12).

In Figure 18 the 1.4 GHz flux is plotted against the broadband X-ray flux. At low redshifts, there are many sources that are strong in the X-ray and weak in the radio. At high redshifts, there is a tendency for AGNs with stronger radio emission to also be strong in the X-ray. The sample has essentially no strong radio sources that are weak in the X-ray (upper-left corner in Figure 18).

#### 4. Summary

We presented a sample of 1744 SDSS DR4 AGNs with X-ray emission from ROSAT PSPC pointed observations. The sample was obtained by positional cross-correlation of all SDSS DR4 AGNs/QSOs (SDSS spectroscopic type 3) with all unique X-ray sources in the catalog of ROSAT pointed observations (WGACAT). Of 1744 X-ray sources, 1,410 (80.9%) are new AGN identifications while the rest are the sources identified in the WGACAT with previously known AGNs. Of 4574 SDSS DR4 AGNs for which we found radio matches in the catalog of the FIRST radio sources, 224 turned up in our sample of X-ray emitting AGNs. We provided the major parameters for the sample objects from the respective catalogs, as well as a number of derived parameters, such as X-ray broadband luminosity, 1.4 GHz radio luminosity, and X-ray hardness ratios. We presented a series of statistical relationships for the sample objects that illustrate their overall properties and demonstrate a high reliability of the X-ray counterpart identification. We plan to make use of the sample data in our subsequent studies of AGNs and starburst galaxies for which the combined optical and X-ray information is crucial.

Funding for the creation and distribution of the SDSS Archive has been provided by the Alfred P. Sloan Foundation, the Participating Institutions, the National Aeronautics and Space Administration, the National Science Foundation, the U.S. Department of Energy, the Japanese Monbukagakusho, and the Max Planck Society. The SDSS Web site is <http://www.sdss.org/>. The SDSS is managed by the Astrophysical Research Consortium (ARC) for the Participating Institutions. The Participating Institutions are The University of Chicago, Fermilab, the Institute for Advanced Study, the Japan Participation Group, The Johns Hopkins University, the Korean Sci-

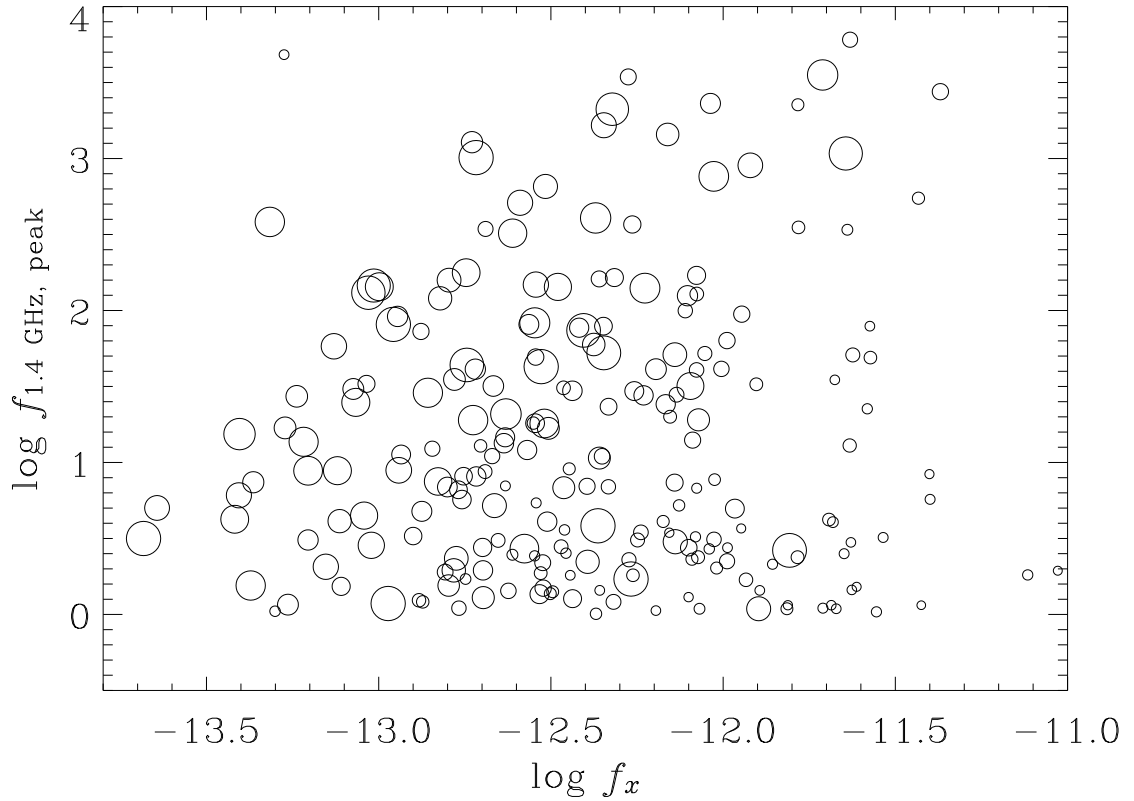


Fig. 18.— The 1.4 GHz flux density (mJy) vs. broadband X-ray flux ( $\text{ergs s}^{-1} \text{cm}^{-2}$ ) for radio-loud X-ray AGNs with counterparts from the FIRST catalog. The symbol size is linearly scaled with redshift, with  $z \leq 0.02$  and  $z \geq 2.3$  corresponding to the smallest and largest symbols, respectively. At low redshifts, there are many weak radio sources that are strong in the X-ray. At high redshifts, the AGNs with stronger radio emission tend to also be strong in the X-ray. Only two weak X-ray emitters are found among strong radio sources.

entist Group, Los Alamos National Laboratory, the Max-Planck-Institute for Astronomy (MPIA), the Max-Planck-Institute for Astrophysics (MPA), New Mexico State University, the University of Pittsburgh, the University of Portsmouth, Princeton University, the United States Naval Observatory, and the University of Washington.

We thank the referee for useful comments and recommendations, which helped us to improve the paper. This research has made use of data obtained from or software provided by the US National Virtual Observatory, which is sponsored by the National Science Foundation.

## REFERENCES

- Abazajian, K., et al. 2005, *AJ*, 129, 1755
- Anderson, S. F. et al. 2003, *AJ*, 126, 2209
- Barger, A. J., Cowie, L. L., Mushotzky, R. F. et al. 2005, *AJ*, 129, 578
- Becker, R. H., White, R. L., & Helfand, D. J. 1995, *ApJ*, 450, 559
- Best, N. P., Kauffmann, G., Heckman, T. M., & Ivezić, Ž. 2005a, *MNRAS*, 362, 9
- Best, N. P., Kauffmann, G., Heckman, T. M., Brinchmann, J., Charlot, S., Ivezić, Ž., & White, S. D. M. 2005b, *MNRAS*, 362, 25
- Brand, K. et al. 2005, *ApJ*, 626, 723
- Brandt, W. N. & Hasinger, G. 2005, *ARA&A*, 43, 827
- Brinkmann, W. et al. 2000, *A&A*, 356, 445
- Brinkmann, W., Yuan, W. & Siebert, J. 1997, *A&A*, 319, 413
- Condon, J.J. et al. 1998, *AJ*, 115, 1623
- Dickey, J. M. & Lockman, F. J. 1990, *ARA&A*, 28, 215
- Fiore, F. et al. 2003, *A&A*, 409, 79
- Green, P. J. et al. 2004, *ApJS*, 150, 43
- Hasinger, G. Miyaji, T., & Schmidt, M. 2005, *A&A*, 441, 417
- Heckman, T. M., Kauffmann, G., Brinchmann, J., Charlot, S., Tremonti, C., & White, S. 2004, *ApJ*, 613, 109
- Hornschemeier, A. E., Heckman, T. M., Ptak, A. F., Tremonti, C. R., & Colbert, E. J. M. 2005, *AJ*, 129, 86
- Imanishi, M. & Wada, K. 2004, *ApJ*, 617, 214
- Kauffmann, G. et al. 2003, *MNRAS*, 346, 1055
- Kim, D.-W. et al. 2004a, *ApJS*, 150, 19
- Kim, D.-W. et al. 2004b, *ApJ*, 600, 59

- McGlynn, T. et al. 2004, ApJ, 616, 1284
- Shen, S., White, S. M. D., Mo, H. J., Voges, W., Kauffmann, G., Tremonti, Ch., Anderson, S. F. 2005, Astro-ph/0512645
- Stark, A. A. et al. 1992, ApJS, 79, 77
- Suchkov, A. A., Hanisch, R. J., & Margon, B. 2005, AJ, 130, No. 6
- Voges, W. et al. 1999, A&A, 349, 386
- Voges, W. et al. 2000, IAU Circ. 7432
- White, R. L., Becker, R. H., Helfand, D. J., & Gregg, M. D. 1997, ApJ, 475, 479
- Wolf, C. et al. 2004, A&A, 421, 913
- Yuan, W., Brinkmann, W., Siebert, J., & Voges, W. 1998, A&A, 330, 108



Table 1. STATISTICS OF THE SDSS-WGACAT-FIRST MATCHES

Source Catalog	Sky Footprint (deg <sup>2</sup> )	$N_{\text{WGACAT}}^{\text{a}}$	$N_{\text{match}}^{\text{b}}$	Spurious <sup>c</sup>
SDSS.....	4783	10396	1744	<5%
WGACAT.....	861	8853	1744	
FIRST <sup>d</sup> .....	4797	862	224	<5%

Note. — The WGACAT sky footprint area is estimated as 0.18 of the footprint area of the SDSS DR4 Spectroscopic Catalog. The FIRST footprint area is assumed to be the same as that of the SDSS.

<sup>a</sup>Estimated number counts in the WGACAT footprint area.

<sup>b</sup>Number of the SDSS–WGACAT and FIRST<sup>d</sup>–WGACAT matching sources in the WGACAT footprint area.

<sup>c</sup>Percentage of spurious associations with X-ray sources; < 2% for 72% of the AGNs, which are within  $\theta = 30$  arcmin.

<sup>d</sup>Only sources matching the SDSS DR4 AGNs are counted.

Table 2. SDSS AGNs WITH X-RAY EMISSION FROM ROSAT PSPC POINTED OBSERVATIONS

SDSS Parameters																
ID	SDSS ID	RA (deg)	Dec (deg)	Redshift	$P_z^a$	MT <sup>b</sup>	$u^c$	$e_u$	$g^c$	$e_g$	$r^c$	$e_r$	$i^c$	$e_i$	$z^c$	$e_z$
56	587725473883357292	162.552597	62.884251	0.201	1.00	3	20.329	0.099	19.033	0.015	18.014	0.009	17.443	0.008	17.293	0.024
57	587725489986535603	253.006348	62.535847	1.633	0.98	6	19.281	0.027	19.087	0.011	19.158	0.013	19.000	0.018	18.969	0.049
58	587725489988042772	255.566803	59.448818	1.169	1.00	6	19.394	0.029	19.289	0.013	19.006	0.012	18.991	0.017	18.980	0.048
59	587725489988108517	255.583603	59.260723	1.798	0.97	6	20.154	0.046	19.739	0.017	19.261	0.014	18.743	0.014	18.449	0.032
68	587725503945310523	254.581360	62.639751	0.703	0.97	6	20.279	0.054	19.762	0.016	19.779	0.022	19.801	0.030	19.726	0.103
X-Ray Source Parameters																
ID	WGACAT ID	$\delta r$ (arcsec)	$\theta$ (arcmin)	$C_{0.1-2.4}$ ( $s^{-1}$ )	$e_{C_{0.1-2.4}}$ ( $s^{-1}$ )	$\log f_x$ ( $\text{ergs cm}^{-2} \text{s}^{-1}$ )	$\log L_x$ ( $\text{ergs s}^{-1}$ )	HR1	HR2							
56	1WGA J1050.1+6253	3	34	0.0169	0.0021	-12.75	43.16	-0.66	0.47							
57	1WGA J1651.9+6232	22	34	0.0439	0.0026	-12.09	45.31	-0.72	-0.23							
58	1WGA J1702.2+5926	38	23	0.0038	0.0007	-13.24	43.98	-0.70	-0.06							
59	1WGA J1702.2+5916	59	30	0.0041	0.0009	-13.20	44.25	-0.81	0.10							
68	1WGA J1658.3+6238	9	10	0.0168	0.0012	-12.52	44.36	-0.39	0.19							
FIRST Radio Source Parameters																
ID	FIRST ID	$f_{\text{peak}}$ (mJy)	$f_{\text{int}}$ (mJy)	rms (mJy)	$\log L_{1.4\text{GHzpeak}}$ ( $\text{ergs s}^{-1} \text{Hz}^{-1}$ )	$\log L_{1.4\text{GHzint}}$ ( $\text{ergs s}^{-1} \text{Hz}^{-1}$ )										
56	10480+63011J	1.710	1.500	0.143	30.178	30.121										
57	16540+62339J	31.830	39.830	0.151	33.117	33.215										
58	17000+59294J	27.240	29.230	0.156	32.818	32.848										
59	17000+59042J	8.820	8.920	0.142	32.623	32.628										
68	17000+62339J	1.490	1.970	0.148	31.169	31.290										

Note. — Only a few lines of the table are shown here as a guide to the table's content and format. The table is available in its entirety in a machine-readable form in the electronic edition of the *Astronomical Journal*

<sup>a</sup>Redshift confidence.

<sup>b</sup>SDSS morphology type, 3 for resolved and 6 for unresolved objects.

<sup>c</sup>Corrected for Galactic reddening (SDSS dereddened magnitudes).